CrossMark

ORIGINAL PAPER

Surface Reactivity of the Vanadium Phosphate Catalyst for the Oxidation of Methane

Torstein Fjermestad[1] · Alexander Genest[1] · Wenqing Li[1] · Gerhard Mestl[2] ·
Notker Rösch[1,3]

Abstract Using density functional theory (DFT), we compared the reactivity of vanadyl pyrophosphate (VPP) (100), α-VOPO$_4$ (100), and δ-VOPO$_4$ (100) for key elementary steps of the transformation of methane, serving also as model for similar steps that might occur for other hydrocarbon species. We examined in analogous fashion the initial and rate-determining homolytic C–H cleavage and the reaction of methoxy species to methanol. According to these calculated results, the system prefers the oxidation state V^{3+} for both types of reactions, thus avoiding the unstable oxidation state V^{2+}. On the three surfaces modelled, either bare or hydrogenated, the models indicate a rather similar reactivity for C–H cleavage whereas methoxy species are energetically preferred over methanol.

✉ Notker Rösch
  roesch@mytum.de

[1] Agency for Science, Technology and Research, Institute of High Performance Computing, 1 Fusionopolis Way, #16-16 Connexis, Singapore 138632, Singapore

[2] Clariant Produkte (Deutschland) GmbH, Waldheimer Str. 13, 83052 Heufeld, Germany

[3] Department Chemie and Catalysis Research Center, Technische Universität München, 85747 Garching, Germany

Keywords Vanadium phosphate · Selective oxidation · Hydrocarbon · Methane oxidation · DFT calculations

1 Introduction

Currently a large fraction of the available methane resources is utilized for power production through combustion [1]. Using methane as feedstock for the production of chemicals is highly desirable as methane resources are vast [1]. Regarding the production of chemicals, methane is mostly used for generating syngas [1–3]. The direct oxidation of methane by molecular oxygen is very desirable. This conversion has been studied extensively for metal oxides as catalysts [1, 4–8]. At high conversion rates, these systems generally show a rather low selectivity to the desired partially oxidized product [1, 9, 10] because it is more difficult to break the first C–H bond of methane than any subsequent one. Therefore, reaction intermediates often are converted more easily [1, 10]. For instance, the yield of formaldehyde in a direct gas-phase oxidation of methane over a heterogeneous catalyst usually is about 3–4% [1]. Such a typical high temperature C–H bond abstraction is reported to be a radical reaction, yielding CH$_3$ radicals [1, 6, 11]. The most successful heterogeneous approaches to methane oxidation are inspired by homogeneous catalytic systems and lead to methanol, e.g. a CuO$_x$ cluster that is embedded in a zeolite [1, 12].

The present work focuses on the partial oxidation of methane over vanadium phosphate (VPO); the reaction products were mainly CO$_x$ and water [13]. The VPO catalyst consists of several phases; vanadium pyrophosphate (VPP) is the predominant one with vanadium in oxidation state 4+. The VPP crystallites show a plate-like shape, where the basal surface corresponds to the (100) bulk termination

[14]. However, it is well-known that the ideal VPP (100) surface termination is not catalytically active. In a major effort, a dynamic structure of various interconverting VPO phases was demonstrated to exist on top of the VPP (100) surface [15–17].

In order to understand the selectivity limitations of this system, a detailed mechanistic insight is necessary. Density functional theory (DFT) calculations have proved to be a useful tool for obtaining such information [18–21], and we therefore carried out a DFT study in order to elucidate the mechanism of partial oxidation of methane on VPO.

Modeling the partial oxidation of methane is a highly complex task, as any of several aspects concerning the surface, e.g., defects, reconstruction, hydrolysis, and re-oxidation [15–17, 22, 23], may be decisive for the selectivity of the target reaction. However, before looking at details, one has to start with a baseline assumption, namely that one of the known surfaces is active and, in some fashion, uses lattice oxygen for the selective oxidation. Assuming that subsequent re-oxidation will replenish the lattice oxygen to reconstitute the catalyst, we decided to model experimentally known features of anaerobic partial oxidation [24].

The dynamic character of the VPO surface and the potential presence of various interconverting phases was also confirmed in studies on the conversion of butane to maleic anhydride which takes place on the same kind of material [15–17]. This variability of the surface turns any modeling into a complex task.

To tackle this complexity in the nature of the actual surface, we started by building models of idealized reference surfaces that may be present in the VPO catalyst. In addition to the ideal VPP (100) surface, we constructed models of the α-VOPO$_4$ (100) and δ-VOPO$_4$ (100) surfaces. These surfaces were chosen because they have been shown to form on the VPP crystallites under reactive conditions [25, 26]. We selected the (100) surfaces for VPP and α-VOPO$_4$ as they can be created by formally cutting the bulk material between the layers. For δ-VOPO$_4$, we chose the analogous cut, as we expect this phase to be formed in situ on the basal surface of a VPP material.

For each of these model surfaces, we explored the intrinsic reactivity in the partial oxidation of methane by examining elementary steps of the process. These steps are: (i) C–H cleavage, formation of (ii) water and (iii) methanol.

2 Method and Models

We carried out density functional theory (DFT) calculations on periodic models, using the program VASP [27–30], and the PBE exchange–correlation functional [31, 32] in combination with the DFT + U approach [33] and the D2 dispersion correction [34]. For the 3d orbitals of vanadium,

we employed U = 2.3 eV, a value that has been shown to reproduce well thermochemical data of vanadium oxide in various oxidation states [35]. Spin polarization was admitted in all calculations, and a Gaussian smearing technique was invoked with a broadening of 0.05 eV [36], eventually extrapolated to zero broadening. The core electrons were treated by the projector augmented-wave (PAW) method [37, 38]. The valence electrons were represented in a plane-wave basis set with a kinetic-energy cut-off of 400 eV. For the most stable intermediates on each of the three surfaces studied, we verified stationary points by a normal-mode analysis. Given the numerous soft vibrational modes, we accepted structures with at most two imaginary frequencies of up to 50i cm^{-1}; with that scenario, test calculations showed total energies to be stable to 1–2 kJ mol^{-1}. For calculating free energies according to standard procedures at 673 K, the temperature typically used in industrial operations [39], we set vibrational frequencies of normal modes to 50 cm^{-1} or, if higher, to their calculated values [40, 41]. For molecules in the gas phase, we used the program Gaussian09 for calculating those correction terms to the energy that are not related to vibrational modes [40, 42].

Starting from the crystal structures of VPP [43], α-VOPO$_4$ [44], and δ-VOPO$_4$ [45], the bulk geometry of each of these systems was optimized, keeping the cell parameters fixed at the experimental values. From these optimized bulk geometries, we constructed slab models by formally cutting perpendicular to the [100] direction and adding 1.5 nm of "vacuum" space between slab replicas. For the layered structures, VPP and α-VOPO$_4$, surfaces parallel to these layers were generated. To reduce artificial interactions between the slab images, a dipole correction pointing normal to the surfaces was added. The grids in k-space were chosen such that their density was similar for the three materials; see below. For the slab calculations, the number of k points in the directions parallel to the surfaces was the same as in the corresponding bulk calculations; in the perpendicular direction, we employed one k point.

For the optimization of bulk VPP (100), we used a 2 × 1 × 2 Γ-centered grid in k-space (6 × 10^{-4}, 6 × 10^{-4}, 5 × 10^{-4} pm^{-1}). The corresponding slab thickness was ~1.2 nm. In all subsequent optimizations, the atoms in the range of 270 pm from the "bottom" of the slab were kept fixed at their optimized bulk positions. Cutting the slab from the bulk generates dangling P–O bonds on both surfaces of the slab, of which those at the "bottom" were saturated with H atoms. During the initial optimization, these H atoms where allowed to relax together with the other atoms. In the subsequent calculations of VPP slab models, these H atoms were fixed at their optimized positions. For the slab models of VPP we used a Γ-centered 2 × 1 × 1 grid in k-space.

In the initial exploration of H adsorption sites, we noticed P=O bonds at the surface to be very reactive; hence, they

can be expected to be saturated quickly by H atoms, available in the experimental environment. Thus, for a more realistic model, the four outward pointing P=O moieties of the original "upper" surface were capped by H atoms, thus mimicking surface phosphoric acid groups in VPO catalysts (Fig. 1a, Fig. S1 of the ESM). Ultimately, the slab model of VPP (100) comprises 168 atoms per unit cell.

For optimizing bulk α-VOPO$_4$, we used a $3 \times 3 \times 3$ Γ-centered k-point grid (4×10^{-4}, 5×10^{4}, 6×10^{-4} pm^{-1}). The slab model comprised three layers, amounting to an overall thickness of 1.1 nm and 42 atoms per unit cell. The atoms in the lower 60 pm range were kept fixed at their optimized bulk positions. The k-point grid of the slab model was $3 \times 3 \times 1$.

For the bulk optimization of δ-VOPO$_4$, the grid in k-space was $3 \times 3 \times 3$ (4×10^{-4}, 4×10^{-4}, 4×10^{-4} pm^{-1}), centered on the Γ point and reduced to $3 \times 3 \times 1$ for the subsequent slab model calculations. That slab was ~1.4 nm thick, measured along the z direction from the highest- to the lowest-lying atoms of the slab. The V and O centers of the "lower" surface, within 160 pm from the bottom, were kept fixed in their

positions as optimized for the bulk. The dangling oxygen centers were capped with hydrogen atoms; their positions were determined as described above for the slab model of VPP. The resulting unit cell of the slab model of δ-VOPO$_4$ comprises 85 atoms. Every other V=O unit in the top layer is oriented approximately parallel to the surface and the bridging oxygen of that V center is pointing in the direction normal to the surface, e.g., see V=O site **δ.6** of Fig. S5 of ESM. After cutting the surface, there would be a dangling bridging O center of this unit and another dangling oxygen atom of a phosphate unit nearby. To saturate the proper ("upper") slab surface, we admitted a surface reconstruction where these surface V=O groups are rotated by ~90° such that the "dangling" oxygen centers of the V=O groups bind to the phosphorus centers, thus turning those dangling oxygen bonds into bridging V–O–P moieties.

During every turnover of this reaction, at least one hydrogen is transferred to the surface that is not necessarily removed by oxidation. Hence, if we assume to model steady-state kinetics, we also have to include in our study hydrogenated models of the three surfaces under study, VPP (100), α-VOPO$_4$ (100), and δ-VOPO$_4$ (100). For VPP (100), this hydrogenation is in addition to the H atoms capping the P=O bonds, see above. Accordingly, for each of the three surfaces VPP, α-VOPO$_4$, and δ-VOPO$_4$, we constructed the corresponding "hydrogenated" model surfaces by placing one H atom on the surface vanadyl site that exhibits the highest H adsorption energy, **v.1**, **α.1**, and **δ.1**, respectively. Labels of sites and complexes will be explained below on their first occurrence; for a general description of the labelling scheme, see Sect. S1 of the ESM. Overall, we aimed at calculating hydrogen adsorption free energies at representative hydrogenated vanadyl units.

In this work, two types of energy quantities are of interest. We calculate the free energy change G_r of a process in which a chemical bond is being formed or broken,

$$G_r(\text{initial} \rightarrow \text{final}) = G_{\text{tot}}(\text{final}) - G_{\text{tot}}(\text{initial}) \qquad (1)$$

from the corresponding total energies. Analogously, we determine the adsorption free energy, G_{ads} of a hydrogen atom as the (formal) reaction free energy of the adsorption process H(g) → **s.**xH from the gas phase:

$$G_{\text{ads}}(\textbf{s.1H}) = G_{\text{tot}}(\textbf{s.1H}) - G_{\text{tot}}(\text{H(g)}) - G_{\text{tot}}(\textbf{s}) \qquad (2)$$

Here **s.1H** represents an H adsorption complex at the adsorption site **1** on one of the surfaces s, s = **v**, **α**, or **δ**. Similarly, we report physisorption energies for A = CH$_3$, CH$_4$, and H$_2$O as such formal reaction energies $G_{\text{ads}}(\textbf{s}.\text{A})$. The label **s**, used by itself, shall refer to a bare surface. In addition, for facilitating the comparison of adsorbate configurations on various surfaces, we will be invoking models without intra-adsorbate interactions, i.e., with co-adsorbates at formally "infinite" separation. To determine the
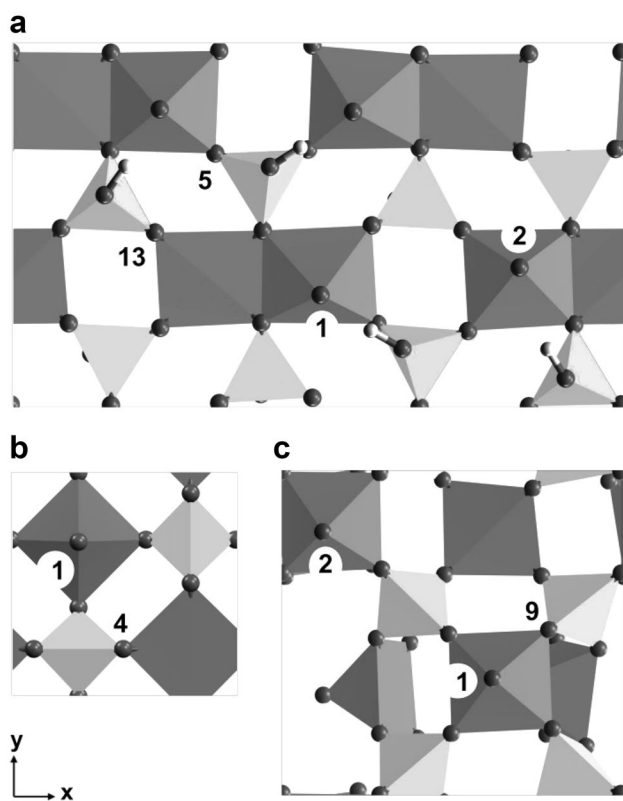

Fig. 1 *Top view* of **a** the VPP (100), **b** the α-VOPO$_4$ (100) and **c** the δ-VOPO$_4$ (100) surfaces with labels of the H adsorption sites. In **a**, the four outward pointing P=O moieties of the original surface are H-capped, i.e. P–OH groups. The bottom layers of the slab models not shown in the panels. V—dark gray polyhedra, P—light gray polyhedra, O—dark gray balls, H—light gray balls

corresponding free energies, one has to calculate separately the adsorption free energies of either species, e.g., for the dissociative adsorption of CH_4 on sites **x** and **y**, one obtains [46]:

$$G_r\left(CH_4 \rightarrow \mathbf{s.xH} + \mathbf{s.yCH_3}\right) = G_{tot}\left(\mathbf{s.xCH_3}\right) + G_{tot}\left(\mathbf{s.yH}\right) - G_{tot}\left(CH_4\right) - 2 \times G_{tot}(\mathbf{s}) \tag{3}$$

3 Results and Discussion

In the following we present our results for modeling important elementary steps of the selective oxidation of methane, namely oxidative dehydrogenation (ODH) as well as the formation of methanol or water on the surfaces VPP (100), α-VOPO$_4$ (100), and δ-VOPO$_4$ (100). For each of the explored reactions we looked at several isomers of intermediate states to gain information about the variability among the sites of a surface. Details of the less stable alternative isomers are presented in Sects. S3, S4, and S5 of the ESM.

ODH comprises two steps [47–49]: (i) a C–H cleavage in which an H atom is transferred from a physisorbed methane molecule to a vacant surface O site, and (ii) a subsequent step where the radical adsorbs on the surface. After the first step, the H atom is strongly bound to a surface O site, and the methyl radical is close to the surface. The C–H cleavage (i) is the kinetically relevant step of all ODH reactions presented in this work [50–52]; it will be discussed in detail in Sect. 3.1 for the three surfaces under study.

When the methyl radical adsorbs on a surface vanadyl O site, a methoxy group emerges. Subsequently, a methanol may form through an H transfer from a nearby hydroxyl group. For the case of methoxy to methanol, this transformation is described in Sect. 3.2. Finally, in Sect. 3.3, we compare the reactivity of the three surfaces examined, using the results obtained thus far, by inspecting various model configuration of adsorption complexes and their transformations, e.g., the preference of 2V–OH vs. V=O+V–OH$_2$.

3.1 C–H Cleavage

The first step of ODH, the C–H cleavage, starts from a physisorbed CH_4 molecule and ends with an H atom adsorbed on an O site and a CH_3 radical in the vicinity of the surface, but not bound to it. Thus the reactivity of the surface, to a large part, is determined by the adsorption free energy, $G_{ads}(H)$, of the site to which the H atom is transferred.

Therefore we calculated $G_{ads}(H)$ for a range of adsorption sites. We labelled the H adsorption structures as **s.xH** (**s = v, α, δ**) for the three surfaces VPP (100), α-VOPO$_4$ (100), and δ-VOPO$_4$ (100), respectively; for details of these adsorption complexes, see Fig. 1 as well as Figs. S1, S2, S3, S4, S5, and S6 of the ESM. The structures of physisorbed methane and

weakly coordinating methyl radicals are labeled **s.CH$_4$** and **s.1 H.CH$_3$**, respectively (Fig. S7 of ESM). The complexes **v.1H, α.1H**, and **δ.1H** have been calculated as the most stable H adsorption structures on the bare surfaces studied (Tables S1, S4, S7 of the ESM); see Sect. S1 of the ESM for a general description of the labelling scheme.

A transfer of hydrogen to a previously hydrogenated vanadyl site, e.g., **v.1H, α.1H, δ.1H**, results in the formation of an adsorbed water molecule. At the reaction temperature of 673 K, the free energy of water desorption is -37.1 kJ mol^{-1} for VPP (100), -13.4 kJ mol^{-1} for α-VOPO$_4$ (100), and 7.7 kJ mol^{-1} for δ-VOPO$_4$ (100). Accordingly, at the assumed reaction conditions, water molecules are (weakly) bound on δ-VOPO$_4$ (100) only.

For determining the free energies of a physisorbed adsorbate molecule (methane), we estimated the entropy $S_{ads}^0(T)$ by scaling the entropy $S_{gas}^0(T)$ of the molecule in the gas phase, at $T = 673$ K, in the spirit of a previous study where this correlation was determined based on experimental values [53]:

$$S_{ad}^0(T) = 0.70 S_{gas}^0(T) - 3.3R \tag{4}$$

The loss of about one-third of the entropy upon adsorption corresponds roughly to the loss of one translational and one rotational degree of freedom, representing motions normal to the surface. In all cases, this resulted in methane adsorption being strongly endergonic (Table 1; Fig. 2). Invoking the energy span model [54, 55], we therefore consider methane in the gas phase as the kinetically relevant starting point of C–H cleavage.

We estimated the free energy G_a of C–H activation by adding the barrier $\Delta = 31.5 \pm 10.5$ kJ mol^{-1} of the backward reaction to the (endergonic) reaction free energy G_r [48, 49]:

$$G_a(CH_4 \rightarrow \mathbf{s.xH.CH_3}) = \Delta + G_r(CH_4 \rightarrow \mathbf{s.xH.CH_3}) \tag{5}$$

We studied these processes on both the bare surfaces and their hydrogenated congeners, e.g., $\mathbf{s = v}$ and **v.1H**, respectively.

3.1.1 The VPP (100) Surface

On the bare VPP (100) surface, H adsorption is notably stronger at the vanadyl O site **v.1**, $G_{ads}(\mathbf{v.1H}) = -218.3$ kJ mol^{-1}, than at the bridging O sites where the highest affinity for an H atom is characterized by $G_{ads}(\mathbf{v.5H}) = -87.5$ kJ mol^{-1} (Table S1 of ESM). For the starting structure of C–H cleavage, physisorbed CH_4, one calculates $G_{ads}(\mathbf{v.CH_4}) = 26.7$ kJ mol^{-1} and $G_r(CH_4 \rightarrow \mathbf{v.1H.CH_3}) = 205.7$ kJ mol^{-1}, Table 1. Note that this reaction free energy is very endergonic because it includes the C–H bond cleavage, calculated at 356 kJ mol^{-1}; see Table S3 of ESM. For C–H cleavage on the bare VPP (100) surface,

Table 1 Free energy values (kJ mol^{-1}) pertaining to the C–H cleavage on bare and hydrogenated surfaces

		Adsorbate configuration[a]	VPP	α-VOPO$_4$	δ-VOPO$_4$
Bare surfaces	CH$_4$ + surface		0.0	0.0	0.0
	CH$_4$, physisorbed	**s.CH$_4$**	26.7	34.6	24.6
	TS(C–H)		237.1	245.5	249.6
	Final state[b] G_r	**s.1H.CH$_3$**	205.7	214.1	218.2
	G_a[c]		237.1	245.5	249.6
Hydrogenated Surfaces	CH$_4$ + surface		0.0	0.0	0.0
	CH$_4$, physisorbed	**s.1H.CH$_4$**	19.1	38.2	27.6
	TS(C–H)		245.3	211.5	197.8
	Final state G_r	**s.1H.1H.CH$_3$**	213.9	180.1	166.4
	G_a[c]		245.3	211.5	197.8

[a] **s = v, α**, or **δ**

[b] The free energy change of the dissociative adsorption of methane also includes the free energy for cleaving a C–H bond, calculated at 356.2 kJ mol^{-1} with the present method

[c] Estimated via Eq. (5)
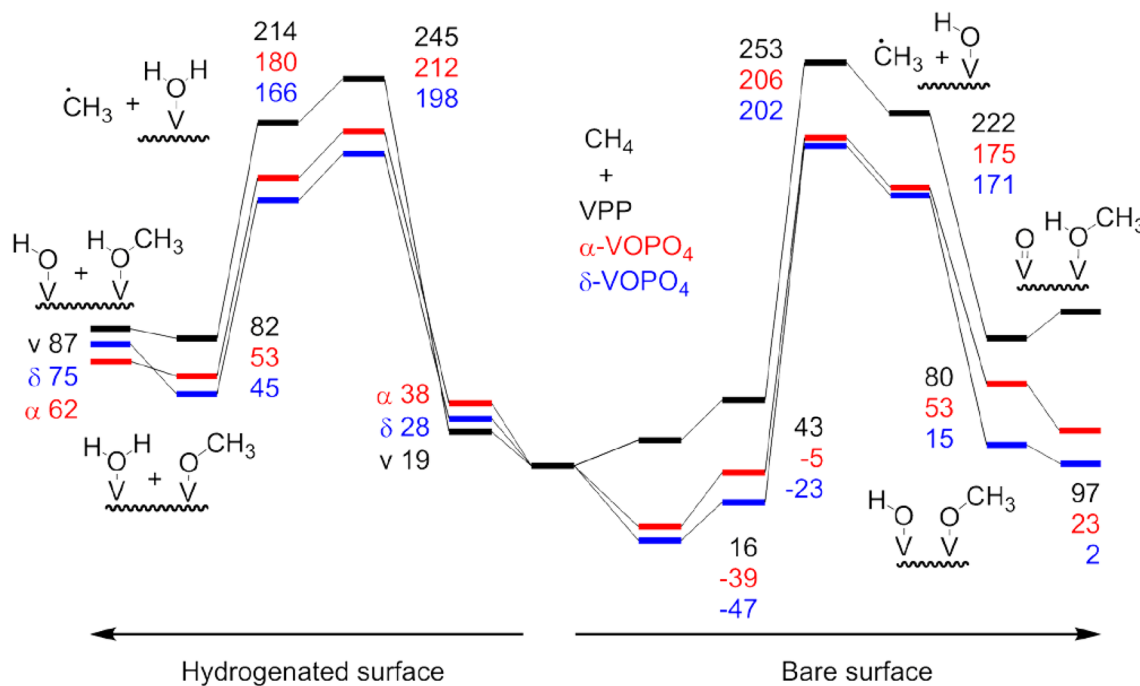
Fig. 2 Free energy profiles (kJ mol^{-1}) for the transformation of CH$_4$ (in the gas phase) to methanol on bare (from the center to the *right*) and hydrogenated surfaces (from the center to the *left*). In each case, the free energies are referenced to a bare surface that carries an adsorbed water molecule at a vanadium center, at formally "infinite" separation; see configuration 2 of Table 2. Thus, on a hydrogenated surface we assume two non-interacting hydrogenated vanadyl groups as shown in configuration 3 of Table 2. For each structure, the energy values are given in a column (from *top* to *bottom*) in the order VPP, α-VOPO$_4$, and δ-VOPO$_4$, except in two cases where the surfaces are explicitly indicated

the activation free energy is estimated at G_a(CH$_4$ → **v.1H. CH$_3$**) = 237.1 kJ mol^1, see Table 1 and Eq. (5).

For the hydrogenated variant of VPP (100), we calculated the adsorption free energy of a physisorbed methane molecule at G_{ads}(**v.1H.CH$_4$**) = 19.1 kJ mol^{-1}. The corresponding final structure, a water molecule at site **v.1** and

a physisorbed methyl species, is reached via the reaction free energy G_r(CH$_4$ → **v.1H.1H.CH$_3$**) = 213.9 kJ mol^{-1}, Table S3 of ESM. Thus, for the activation of methane on the hydrogenated surface VPP (100), one calculates the activation free energy G_a(CH$_4$ → **v.1H.1H. CH$_3$**) = 245.3 kJ mol^{-1}, Table 1.

3.1.2 The α-VOPO$_4$ (100) Surface

Only the adsorption sites on the upper face of the top layer, **α.1** and **α.4**, are available for a direct hydrogen transfer from methane, see Fig. 1b. The resulting adsorption free energies are determined at −190.9 and −152.9 kJ mol^{-1}, respectively. For the encounter complex preceding C–H cleavage, physisorbed CH$_4$, one determines G_{ads}(**α.CH$_4$**) = 34.6 kJ mol^{-1} (Table 1); the pertinent final structure, with the CH$_3$ radical in the gas phase, is reached via G_r(CH$_4$ → **α.1H.CH$_3$**) = 214.1 kJ mol^{-1} (Table 1). Thus, for C–H cleavage at the site **α.1**, one arrives at the activation free energy G_a(CH$_4$ → **α.1H.CH$_3$**) = 245.5 kJ mol^{-1}, Table 1. C–H cleavage on the hydrogenated α-VOPO$_4$ (100) surface starts from **α.1H.CH$_4$**, G_{ads}(**α.1H.CH$_4$**) = 38.2 kJ mol^{-1}, and ends at **α.1H.1H.CH$_3$**, G_r(CH$_4$ → **α.1H.1H.CH$_3$**) = 180.1 kJ mol^{-1}, with a free energy barrier G_a(CH$_4$ → **α.1H.1H.CH$_3$**) = 211.5 kJ mol^{-1}, Table 1.

3.1.3 The δ-VOPO4 (100) Surface

Again, only sites located at the surface are available for splitting the C–H bond of a reacting methane molecule. Accordingly, we identified site **δ.1** as the preferred site for H adsorption, with G_{ads} (**δ.1H**) = −203.4 kJ mol^{-1} (Fig. 1c and Table S7 of ESM). The corresponding state of physisorbed methane, **δ.CH$_4$**, is characterized by G_{ads}(**δ.CH$_4$**) = 24.6 kJ mol^{-1}. For the energetics of C–H cleavage we obtained G_r(CH$_4$ → **δ.1H.CH$_3$**) = 218.2 kJ mol^{-1} and G_a(CH$_4$ → **δ.1H.CH$_3$**) = 249.6 kJ mol^{-1}, Table 1. On the hydrogenated δ-VOPO$_4$ (100) surface we computed the physisorption of CH$_4$ at **δ.1H**, with G_{ads}(**δ.1H.CH$_4$**) = 27.6 kJ mol^{-1}. The final state of C–H cleavage exhibits G_r(CH$_4$ → **δ.1H.1H.CH$_3$**) = 166.4 kJ mol^{-1} and G_a(CH$_4$ → **δ.1H.1H.CH$_3$**) = 197.8 kJ mol^{-1}, Table 1.

3.1.4 Comparison of the Surfaces

Among the bare surfaces studied, VPP (100), α-VOPO$_4$ (100), and δ-VOPO$_4$ (100), VPP (100) is slightly more reactive than α-VOPO$_4$ (100) and δ-VOPO$_4$ (100), as expressed by the corresponding free energy barriers G_a = 237.1, 245.5, and 249.6 kJ mol^{-1}, respectively. This trend is changed for reactions on hydrogenated surfaces. There, both V^{5+} phases with their activation free energies, G_a = 211.5 kJ mol^{-1} [α-VOPO$_4$ (100)] and G_a = 197.8 kJ mol^{-1} [δ-VOPO$_4$ (100)] are significantly more reactive than the V^{4+} phase VPP, with G_a = 245.3 kJ mol^{-1}. The high free energy activation barriers are mainly caused by the loss of entropy upon CH$_4$ adsorption. At 673 K, the free energy correction of the

s.1H.1H.CH$_3$ and s.1H.CH$_3$, s = v, α, δ, structures varies from 65 to 95 kJ mol^{-1}.

C–H cleavage on the bare surfaces is accompanied by the hydrogenation of a vanadyl group, V=O. On a hydrogenated surface, the analogous process occurs at an already hydrogenated vanadyl group, VOH, thus resulting in an adsorbed water molecule. For VPP, the oxidation state of the participating V centers changes from 4+ to 3+ on the bare surface and from 3+ to 2+ on the hydrogenated surface. For α-VOPO$_4$ and δ-VOPO$_4$, the V oxidation state changes from 5+ to 4+ on the bare surface and from 4+ to 3+ on the hydrogenated surface. Our results indicate oxidation state 3+ to be preferred over 2+ and 4+.

3.2 Adsorption of Methyl and Formation of Methanol

As outlined at the start of Sect. 3, the second step of the ODH is an adsorption of a methyl radical on a vacant site. To identify the resulting structures, we follow the general labelling scheme (Sect. S1 of ESM) by indicating the adsorption site of methyl as **y**, e.g., **s.xH.yCH$_3$**. As adsorption site **x** for hydrogen, we chose the most stable accessible sites, as determined in Sect. 3.1, **v.1** for VPP, **α.1** for α-VOPO$_4$, and **δ.1** for δ-VOPO$_4$, see Fig. 1.

Methyl adsorption on a vanadyl oxygen results in the formation of a methoxy structure. This adsorption mode turned out to be most favorable for VPP and α-VOPO$_4$ surfaces while δ-VOPO$_4$ showed a comparable stability for methyl adsorption on vanadyl O sites and bridging O sites, see Sects. S3 to S6 of ESM. Starting from the methoxy structure, a methanol molecule may form through a hydrogen transfer from a nearby hydroxyl group. Despite the high propensity for methanol desorption from the surface at 673 K [VPP (100): −61.5 kJ mol^{-1}, α-VOPO$_4$ (100): −12.5 kJ mol^{-1}, δ-VOPO$_4$ (100): 7.9 kJ mol^{-1}], we chose to compare free energies of structures where a methanol molecule is adsorbed on the surface, in analogy to the situation where a water molecule is formed; see Sect. 3.1.

As on the corresponding bare surfaces, we also studied for hydrogenated surfaces the formation of methoxy species, followed by a subsequent transformation to methanol on the same sites. Yet, the hydrogen atom to be transferred originates from an adsorbed water molecule at the initial vanadyl site. Recall that only a water molecule at these sites is an unstable intermediate, except on δ-VOPO$_4$ (Sect. 3.1).

3.2.1 The VPP (100) Surface

A methyl radical adsorbs in considerably less endergonic fashion on vanadyl oxygen at site **v.2**, G_r(CH$_4$ → **v.1H.2CH$_3$**) = 63.9 kJ mol^{-1} than on a bridging oxygen center **v.13**, e.g. G_r(CH$_4$ → **v.1H.13CH$_3$**) = 232.4 kJ mol^{-1} (Table S3, Fig. 1a and Fig. S2 of ESM). If methyl adsorbs

on the same vanadyl site as the H atom, an adsorbed methanol molecule is formed, e.g., at the site **v.1**, $G_r(CH_4 \rightarrow$ **v.1H.1CH$_3$**$) = 87.1$ kJ mol^{-1}, or **v.2**, $G_r(CH_4 \rightarrow$ **v.2H.2CH$_3$**$) = 80.9$ kJ mol^{-1}, Table S3 of ESM. Thus, the transformation of a methoxy species (**v.1H.2CH$_3$**) to methanol (**v.2H.2CH$_3$**) is only slightly endergonic, $G_r($**v.1H.2CH$_3$** $\rightarrow$ **v.2H.2CH$_3$**$) = 17.0$ kJ mol^{-1}.

When one aims at describing the formation of a methoxy species on the hydrogenated VPP (100) surface, one has to deal with a situation that comprises three adsorbates. For instance, one starts from the adsorbate configuration **v.1H.1H.2CH$_3$** where a water molecule is adsorbed at **v.1**, see Fig. 1a. This complex can be viewed as having originated from two-fold hydrogenation of vanadyl site **v.1**. On the hydrogenated VPP (100) surface, we determined a value for the corresponding formation free energy, $G_r(CH_4 \rightarrow$ **v.1H.1H.2CH$_3$**$) = 82.4$ kJ mol^1, that is slightly larger than on the bare surface, $G_r(CH_4 \rightarrow$ **v.1H.2CH$_3$**$) = 63.9$ kJ mol^{-1}. Methanol may form via H transfer from an adsorbed water molecule, **v.1H.1H**, to the methoxy moiety at vanadyl site **v.2**, in an essentially thermoneutral process, $G_r($**v.1H.1H.2CH$_3$** $\rightarrow$ **v.1H.2H.2CH$_3$**$) = 4.7$ kJ mol^{-1}, Table S3 of ESM.

3.2.2 The α-VOPO₄ (100) Surface

The adsorption of methyl and H on the same vanadyl oxygen site **α.1** (Fig. 1b) results in an adsorbed methanol, **α.1H.1CH$_3$**, $G_r(CH_4 \rightarrow$ **α.1H.1CH$_3$**$) = 61.6$ kJ mol^{-1}. Adsorbing methyl and H on two isolated sites **α.1, α.1H + α.1CH$_3$**, at formally "infinite" separation, is more endergonic, $G_r(CH_4 \rightarrow$ **α.1H + α.1CH$_3$**$) = 91.6$ kJ mol^{-1}. This allows an alternative pathway to methanol, **α.1H + α.1CH$_3$** $\rightarrow$ **α.1H.1CH$_3$**, that is analogous to the situation on VPP where we discussed two vanadyl oxygen sites in one unit cell. The formation of methanol on α-VOPO₄ (100) is exergonic, $G_r($**α.1H + α.1CH$_3$** $\rightarrow$ **α.1H.1CH$_3$**$) = -30.0$ kJ mol^{-1}, in contrast to VPP (100) where the formation of methanol is endergonic. This contrasting behavior is related to the formation of the stable oxidation state V^{3+} for α-VOPO₄ at variance with VPP, where this reaction results in the formation of a V^{2+} species.

For the hydrogenated α-VOPO₄ (100) surface, one calculates a reaction free energy $G_r(CH_4 +$ **α.1H + α** $\rightarrow$ **α.1H.1H + α.1CH$_3$**$) = 52.5$ kJ mol^{-1} for converting methane into adsorbed methoxy and an adsorbed water molecule at separated, non-interacting vanadyl sites. We used this adsorption at formally "infinite" separation as the unit cell for the α-VOPO₄ (100) surface does not contain a second surface vanadyl oxygen, i.e., the preferred binding site for both adsorbates. Keeping the subsequent formation of methanol as analogous as possible to the corresponding process on the bare surface, methanol may easily be formed via H transfer from a water molecule to a methoxy species, **α.1H.1H +**

α.1CH$_3$ $\rightarrow$ **α.1H + α.1H.1CH$_3$**, as the associated reaction energy is calculated at 9.0 kJ mol^{-1}. Note that this process is much more facile that when it occurs in a direct fashion, from methane in the gas phase where $G_r(CH_4 +$ **α.1H + α** $\rightarrow$ **α.1H.1CH$_3$ + α.1H**$) = 61.6$ kJ mol^{-1}, Table S6 of ESM. Here, the final adsorbate structure, **α.1H.1CH$_3$ + α.1H** (methanol + OH), involves non-interacting sites, i.e. in two unit cells at formally "infinite" separation.

3.2.3 The δ-VOPO4 (100) Surface

The formation of methanol is endergonic at the vanadyl site **δ.1** (Fig. 1c), $G_r(CH_4 \rightarrow$ **δ.1H.1CH$_3$**$) = 29.1$ kJ mol^{-1}, and even more so at the vanadyl site **δ.2**, $G_r(CH_4 \rightarrow$ **δ.2H.2CH$_3$**$) = 48.9$ kJ mol^{-1}. The strongest adsorption with hydrogen and methyl adsorbed at different sites is even more endergonic, $G_r(CH_4 \rightarrow$ **δ.1H.2CH$_3$**$) = 62.1$ kJ mol^{-1}. In consequence, the formation of methanol from the latter intermediate **δ.1 H.2CH$_3$** on δ-VOPO₄ (100) is exergonic, $G_r($**δ.1 H.2CH$_3$** $\rightarrow$ **δ.2 H.2CH$_3$**$) = -13.2$ kJ mol^{-1}.
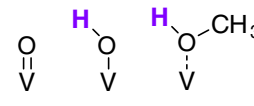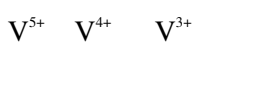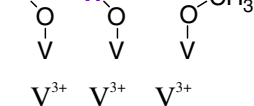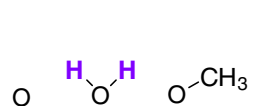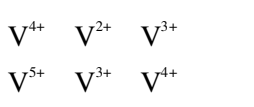
For the corresponding hydrogenated surface δ-VOPO₄ (100), we identified the structures **δ.1H.1H.2CH$_3$** and **δ.1H.1H.9CH$_3$** as least unstable, formed from CH$_4$ + **δ.1** with reaction free energies of 45.0 kJ mol^{-1} and 52.8 kJ mol^{-1}, respectively. The former adsorption complex is analogous to the structure **δ.1H.2CH$_3$** on the bare δ-V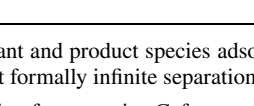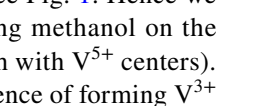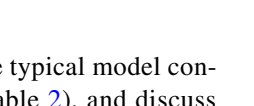OPO₄ surface. The process where methanol forms via H transfer from a water molecule to a methoxy structure, is endergonic by 30.4 kJ mol^{-1}, yielding **δ.1H.2H.2CH$_3$**. As on the surface α-VOPO₄ (100), this transformation among surface species is again much more facile than when the reaction occurs directly for methane from the gas phase, CH$_4$ + **δ.1** $\rightarrow$ **δ.1H.2H.2CH$_3$** where the reaction free energy is 75.4 kJ mol^{-1}, Table S9 of ESM.

3.2.4 Comparison of the Surfaces

For VPP, the formation of methanol from the methoxy species is endergonic for the bare surface (17.0 kJ mol^{-1}) and essentially thermoneutral for the hydrogenated surface (4.7 kJ mol^{-1}). For α-VOPO₄ and δ-VOPO₄, the situation is reversed with the methanol formation being exergonic on the bare surfaces, −30.0 and −13.2 kJ mol^{-1}, respectively, and endergonic on the hydrogenated surfaces, 9.0 and 30.4 kJ mol^{-1}, respectively. One may rationalize this trend with the presence of V^{3+} species being associated with a stable structure. The oxidation states of the different structures are shown schematically in Table 2.

Comparing the surfaces for the case that both species, H and CH$_3$, adsorb at the same site **u**, we determined the reaction energy $G_r(CH_4 \rightarrow$ **s.uH.uCH$_3$**$)$ at 80.9 kJ mol^{-1} for VPP (**u = 2**), 61.6 kJ mol^{-1} for α-VOPO₄ (**u = 1**), and

Table 2 Initial and final states of adsorption complexes on the surfaces VPP (100), α-VOPO$_4$ (100), and δ-VOPO$_4$ (100), as well as the corresponding reaction energies G_r (kJ mol^{-1}): $1 \rightarrow 2$—formation of a methoxy species from methanol, $1 \rightarrow 3$—formation of a water molecule from methanol on a hydrogenated surface

n	Surface state[a]	Surface	Sites[a]	G_r[b]
1	H–O–V, H–O–V, CH$_3$–O–V (O=V)			
	V^{4+} V^{3+} V^{2+}	VPP	$v + v.1H + v.2H.2CH_3$	–
	V^{5+} V^{4+} V^{3+}	α-VOPO$_4$	$\alpha + \alpha.1H + \alpha.1H.1CH_3$	–
		δ-VOPO$_4$	$\delta + \delta.1H + \delta.2H.2CH_3$	–
2	H–O–V, H–O–V, CH$_3$–O–V			
	V^{3+} V^{3+} V^{3+}	VPP	$2 \times v.1H + v.2CH_3$	−28.9
	V^{4+} V^{4+} V^{4+}	α-VOPO$_4$	$2 \times \alpha.1H + \alpha.1CH_3$	30.0
		δ-VOPO$_4$	$2 \times \delta.1H + \delta.2CH_3$	1.0
3	O=V, H–O–V–H, CH$_3$–O–V			
	V^{4+} V^{2+} V^{3+}	VPP	$v + v.1H.1H + v.2CH_3$	−13.0
	V^{5+} V^{3+} V^{4+}	α-VOPO$_4$	$\alpha + \alpha.1H.1H + \alpha.1CH_3$	−9.0
		δ-VOPO$_4$	$\delta + \delta.1H.1H + \delta.2CH_3$	−46.3

[a]Reactant and product species adsorbed at the sites listed (depicted from left to right) on the various surfaces at formally infinite separation

[b]Reaction free energies G_r for reactions $1 \rightarrow 2$ and $1 \rightarrow 3$

29.1 kJ mol^{-1} for δ-VOPO$_4$ ($u = 1$), see Fig. 1. Hence we note a stronger propensity for forming methanol on the surfaces α-VOPO$_4$ and δ-VOPO$_4$ (both with V^{5+} centers). This is another example for the preference of forming V^{3+} species, e.g., when methanol is formed on the bare surfaces α-VOPO$_4$ and δ-VOPO$_4$.

3.3 Transformations of Model Adsorbate Configurations

In the following, we will assume three typical model configurations of adsorbates, $n = 1$–3 (Table 2), and discuss the energetics of the transformations $1 \rightarrow 2$, $1 \rightarrow 3$, and $2 \rightarrow 3$ between these surface "states". The model configurations comprise the adsorbates methanol, water, or methoxy, formally without direct intra-adsorbate interactions (at "infinite" separations) to allow a direct comparison of the three surfaces **s** under study [**s** = VPP (100), α-VOPO$_4$ (100), or δ-VOPO$_4$ (100)]; note that our model of α-VOPO$_4$ exhibits only one surface vanadyl group per unit cell.

3.3.1 Formation of a Water Molecule from Isolated VOH Groups

One may determine the formation free energy of a water molecule on the surface as free energy difference $G_r(\mathbf{s.}$ $\mathbf{xH + s.xH} \rightarrow \mathbf{s + s.xH.xH}) = G_{ads}(\mathbf{s.xH.xH}) - G_{ads}(\mathbf{s.}$ $\mathbf{xH})$ between hydrogen desorption from a site **s.xH**, and hydrogen adsorption to form **s.xH.xH**. For the two hydrogen adsorption events on the VPP surface, we calculated $G_{ads}(\mathbf{v.1H}) = -218.3$ kJ mol^{-1} and $G_{ads}(\mathrm{H} \rightarrow$ $\mathbf{v.1H.1H}) = -202.4$ kJ mol^{-1}, hence $G_r(\mathbf{v.1H + v.1H} \rightarrow$ $\mathbf{v.1H.1H}) = 15.9$ kJ mol^{-1}; see Reaction $2 \rightarrow 3$ on VPP, Table 2. For the surfaces α-VOPO$_4$ (100) and δ-VOPO$_4$ (100), one obtains in similar fashion $G_r(\mathbf{\alpha.1H + \alpha.1H} \rightarrow \mathbf{\alpha}$ $\mathbf{.1H.1H}) = -39.1$ kJ mol^{-1} and $G_r(\mathbf{\delta.1 + \delta.1} \rightarrow \mathbf{\delta.1H.1H})$ $= -47.3$ kJ mol^{-1}, Table 2. Thus, forming water molecules in this way is exergonic for α-VOPO$_4$ (100) and δ-VOPO$_4$ (100), in contrast to VPP (100).

A surface with V=O and V–OH$_2$ groups likely has similar C–H cleavage capabilities as a bare surface. In the following, we therefore use the energetics of the process $\mathbf{s.1H + s.1H} \rightarrow \mathbf{s.1H.1H}$ as an estimate of the relative

stability of a hydrogenated and a bare surface; see Reaction 2 → 3, Table 2.

3.3.2 From Methane to Methanol

Next, we combine the discussed processes into a complete reaction profile for the transformation of methane to the corresponding alcohol, Fig. 2. Note we will be comparing the surface states 2 and 3 as just introduced, Table 2. Based on the energy span model [54, 55], we note that the stability of the surfaces affects the overall C–H cleavage reactivity. Comparing the reactivity of hydrogenated and bare surfaces, we see that for all three surfaces, the reactivity trend is somewhat compensated by the surface stability.

For the bare surfaces, the lower stability of VPP (100) results in a similar reactivity of VPP, α-VOPO$_4$ and δ-VOPO$_4$, the largest difference being just 7.5 kJ mol^{-1}. For the hydrogenated surfaces, the difference in surface stability causes the reactivity to differ at most 5.3 kJ mol^{-1}. In conclusion, all surfaces show similar activation free energies for C-H cleavage both in the bare and the hydrogenated states. Furthermore, we note that for the final state, i.e. adsorbed methanol, the oxidized surfaces α-VOPO$_4$ and δ-VOPO$_4$ are by 39 and 74 kJ mol^{-1} more stable in the bare state than in the hydrogenated state, Fig. 2. The opposite holds for VPP; in the bare state, adsorbed methanol is by 10 kJ mol^{-1} less stable than in the hydrogenated state. We rationalize this trend as described in the previous section, by reference to the free energy preference between 2V–OH vs. V=O + V-OH$_2$.

3.3.3 Stability of Methoxy and Methanol Adsorbates

Finally, we address the stability of surface methoxy moieties from the respective most favorable adsorption complexes, again without direct interaction (Table 2).

For VPP, the conversion of methanol to methoxy and hydroxyl, reaction 1 → 2, is thermodynamically preferred, $G_r = -28.9$ kJ mol^{-1}, over the conversion to methoxy and water, reaction 1 → 3, $G_r = -13.0$ kJ mol^{-1}, Table 2. For α-VOPO$_4$, the formation of water from methanol, reaction 1 → 3, is favored, $G_r = -9.0$ kJ mol^{-1}, over the formation of methoxy and hydroxyl, reaction 1 → 2, $G_r = 30.0$ kJ mol^{-1}. For δ-VOPO$_4$, the trends are the same, but more pronounced; the formation of water and methoxy, reaction 1 → 3, is strongly exergonic, $G_r = -46.3$ kJ mol^{-1}, whereas the formation of methoxy and hydroxyl, reaction 1 → 2, is essentially thermoneutral, $G_r = 1.0$ kJ mol^{-1}.

As done several times before, one can rationalize the energetics of the reactions 1 → 2 and 1 → 3 by the stability preference for the oxidation state 3+ of the V centers. In surface state 2 of VPP, all three V centers are in oxidation state 3+ whereas surface state 3 features only one such center. Thus, one concludes that state 2 is preferred over state 3. In

surface state 2 of α-VOPO$_4$ and δ-VOPO$_4$, all three V centers in oxidation state 4+ whereas in state 3 one center is in oxidation state 3+. Therefore, state 3 should be favored over state 2 in this case.

Above, we concluded that methoxy species are favored on a reduced surface (VPP). For the oxidized surfaces α-VOPO$_4$ and δ-VOPO$_4$, we noted the opposite situation: methoxy species are significantly less stable than alcohol species. Yet, methoxy species are preferred by at least 9 kJ mol^{-1} also for oxidized surfaces when co-adsorbed hydrogen forms water molecules instead of hydroxyls on the surface; see reaction 1 → 3, Table 2. The formation of methoxy species was calculated exergonic for all surfaces; see reactions 1 → 2 and 1 → 3 in Table 2.

3.3.4 Comments on the Calculated Free Energy Barriers

The free energy barriers as determined in this study using a PBE + U approach are relatively high, from 219 to 281 kJ mol^{-1}, deserving some comments. *Free energy* barriers on oxidative dehydrogenation reactions have to be higher than the corresponding *activation energies* because the entropy of the gas-phase hydrocarbon species is lost exactly in this step. Even the mildly exothermic formation of an encounter complex does not help in this regard as the associated free energy change will be notably endergonic, Table 1, due to the associated significant loss of the entropy contributions of translational and rotational degrees of freedom. Regarding the absolute values of these barriers, it is informative to compare to values calculated for C–H activation of methane or other hydrocarbons by other vanadyl species. Using the hybrid B3LYP DFT approach to account for possible self-interaction artifact (instead of the PBE + U method applied here), free energy barriers of 259 and 280 kJ mol^{-1} have been determined for the C–H activation of CH$_4$ (at 800 K) over a silsesquioxane bound V=O moiety and a O=V(OH)$_3$ species [4]. Furthermore, a free energy barrier for ODH of propene at 600 K on a silsesquioxane, where two Si–H were substituted by V=O moieties, was calculated at 224 kJ mol^{-1}, using the same computational method [56]. These calculated free energy barriers of ODH at V=O units in various environments are quite comparable to those obtained in the present work (at 673 K). Another B3LYP study [57], using a V$_4$O$_{10}$ cluster as a model for vanadium pentoxide, V$_2$O$_5$, determined for methane ODH an *energy* barrier of 143 kJ mol^{-1}, quite similar to the *energy* barriers of 121–169 kJ mol^{-1} calculated in the present work for methane ODH over vanadium phosphate. In addition, the C–H activation energies of a secondary carbon center of propane over all previously mentioned models, V=O substituted into a silsesquioxane, O=V(OH)$_3$, V$_4$O$_{10}$, and even on V$_3$O$_7^+$ (using B3LYP calculations) as well as on a periodic V$_2$O$_5$ model (using PBE calculations) were also in

this range, 100–143 kJ mol^{-1} [4, 47, 57, 58]. Only for the hydrogenation of the uncapped P=O unit on the extremely reactive X1 surface of VOPO$_4$ notably lower *energy* barriers, 57–59 kJ mol^{-1}, have been reported from PBE calculations for ODH of butane [49]. Note, however, that the semi-local PBE functional may be prone to self-interaction artifacts.

4 Conclusion

Using DFT model calculations, we probed various surfaces of the vanadium phosphate catalyst for the oxidation of methane. In particular, we examined the reactivity for C–H cleavage and methanol formation on the (100) surfaces of vanadyl pyrophosphate VPP, as well as on the (100) surfaces of the two phases α-VOPO$_4$ and δ-VOPO$_4$ of vanadyl orthophosphate. For the C–H cleavage on hydrogenated model surfaces, we calculated lower free energy barriers by 34 kJ mol^{-1} (α-VOPO$_4$) and 48 kJ mol^{-1} (δ-VOPO$_4$) for the oxidized surfaces compared to the reduced surface VPP. This trend of the free energy values is essentially cancelled out when the stability of the surfaces is taken into account. Then the energy span for the barrier of C–H cleavage for VPP is by no more than 5.3 kJ mol^{-1} lower than for the oxidized surfaces, Fig. 2 [54, 55]. Among the bare surfaces, VPP (100) is slightly more active for the C–H cleavage than the oxidized surfaces α-VOPO$_4$ and δ-VOPO$_4$ if one neglects the stability of the surfaces; the barriers on the latter two surfaces are by 8.4 and 12.5 kJ mol^{-1} higher. When the stability of the surfaces is accounted for, VPP is by at least 3.4 kJ mol^{-1} less reactive (as measured by the energy span) than the oxidized surfaces. To rationalize these findings, one may, again, refer to the calculated high stability of vanadium in oxidation state 3+ and the low stability of vanadium in oxidation state 2+.

This stability trend can also be used for rationalizing the formation of methoxy and methanol species on the three surfaces examined. Methanol formation on VPP (100) requires the reduction to V^{2+} and therefore methoxy formation is favored, by −28.9 kJ mol^{-1}. For α-VOPO$_4$ (100) and δ-VOPO$_4$ (100), intermediate adsorption complexes comprising V^{3+} species were calculated significantly more stable than complexes with vanadium in other oxidation states. Among the V^{3+} species, methoxy adsorption complexes were calculated to be by at least 9.0 kJ mol^{-1} more stable than complexes of methanol, when the leaving hydrogen is adsorbed at a hydroxyl group, forming water.

The above discussion shows that most trends of the present results can be rationalized by a preference for V centers to reduce to oxidation state 3+. Experimentally, the oxidation state of vanadium centers has been determined by X-ray photoelectron spectroscopy (XPS) [59, 60]. XPS studies on VPO catalysts under ultra-high vacuum conditions indicated

a mixture of oxidation states 4+ and 5+ for the surface V centers [61]. Low pressure increases the propensity for eliminating O atoms from the surface, thus reducing the ratio V^{5+}/V^{4+}. In an in situ XPS study on two VPO catalysts [62], Kleimenov et al. fed *n*-butane in the presence of O$_2$, and determined the oxidation state of surface V centers to be 4+ for both catalysts. The lower reaction rate in the absence of O$_2$ was rationalized by the limited oxygen transport from the bulk to the surface. In these studies, no reduction of V centers beyond V^{4+} was observed [62].

To the best of our knowledge, V^{3+} centers have not been identified in VPO materials under catalytic conditions. This discrepancy to our computational results can be rationalized by assuming that any re-oxidation of V^{3+} centers by bulk oxygen atoms or O$_2$ from air is a rather fast process. Note also that in the present work, we only described the reduction of vanadium, bypassing any re-oxidation processes.

To conclude, some comments seem appropriate regarding C–H activation in general over the VPO catalyst. In particular, this catalyst is used for the conversion of butane to maleic anhydride as indicated above [63–66]. This reaction is also assumed to proceed via an initial radicalic ODH step, analogous to the first step explored in the present study [47], followed by the adsorption of a hydrocarbon radical at the surface of the catalyst. The results obtained here are also relevant to the radicalic initial activation of butane as the enthalpy of C–H bond activation of *n*-butane is experimentally only by ~28 kJ mol^{-1} (or ~7%) lower than that of methane, ~439 kJ mol^{-1} [67].

The results of the present mechanistic model study hopefully laid the foundation for further experimental and computational work directed at improving the selectivity of the VPO system through rational catalyst design.

References

1. Horn R, Schlögl R (2015) Catal Lett 145:23–39
2. Aasberg-Petersen K, Dybkjær I, Ovesen CV, Schjødt NC, Sehested J, Thomsen SG (2011) J Nat Gas Sci Eng 3:423–459
3. Rostrup-Nielsen JR, Sehested J, Nørskov JK (2002) Adv Catal 47:65–139
4. Rozanska X, Sauer J (2008) Int J Quantum Chem 108:2223–2229
5. Kwapien K, Paier J, Sauer J, Geske M, Zavyalova U, Horn R, Schwach P, Trunschke A, Schlögl R (2014) Angew Chem Int Ed 53:8774–8778
6. Cooper CA, Hammond CR, Hutchings GJ, Taylor SH, Willock DJ, Tabata K (2001) Catal Today 71:3–10
7. Kumar G, Lau S, Krcha MD, Janik MJ (2016) ACS Catal 6:1812–1821
8. Haber J, Witko M (2003) J Catal 216:416–424

9. Zavyalova U, Holena M, Schlögl R, Baerns M (2011) Chem-CatChem 3:1935–1947
10. Labinger JA (1988) Catal Lett 1:371–375
11. Driscoll DJ, Martir W, Wang JX (1985) J Am Chem Soc 107:58–63
12. Groothaert MH, Smeets PJ, Sels BF, Jacobs PA, Schoonheydt RA (2005) J Am Chem Soc 127:1394–1395
13. McCormick RL, Alptekin GO, Herring AM, Ohno TR, Dec SF (1997) J Catal 172:160–169
14. Inumaru K, Okuhara T, Misono M (1992) Chem Lett 10:1955–1958
15. Cavani F, Santi DD, Luciani S, Lofberg A, Bordes-Richard E, Cortelli C, Leanza R (2010) Appl Catal A 376:66–75
16. Cavani F, Luciani S, Esposti ED, Cortelli C, Leanza R (2010) Chem Eur J 16:1646–1655
17. Bluhm H, Hävecker M, Kleimenov E, Knop-Gericke A, Liskowski A, Schlögl R, Su DS (2003) Top Catal 23:99–107
18. Orio M, Pantazis DA, Neese F (2009) Photosynth Res 102:443–453
19. Ziegler T, Autschbach J (2005) Chem Rev 105:2695–2722
20. Greeley J, Nørskov JK, Mavrikakis M (2002) Annu Rev Phys Chem 53:319–348
21. Moskaleva L, Chiu C-C, Genest A, Rösch N (2016) Chem Rec. doi:10.1002/tcr.201600048
22. Zanthoff HW, Sananes-Schultz M, Buchholz SA, Rodemerck U, Kubias B, Baerns M (1998) Appl Catal A 172:49–58
23. Haras A, Witko M, Salahub DR, Duarte HA (2003) Surf Sci 538:160–170
24. Wang D, Barteau MA (2001) J Catal 197:17–25
25. Koyano G, Yamaguchi F, Okuhara T, Misono M (1996) Catal Lett 41:149–152
26. Koyano G, Okuhara T, Misono M (1998) J Am Chem Soc 120:767–774
27. Kresse G, Hafner J (1993) Phys Rev B 47:558–561
28. Kresse G, Hafner J (1994) Phys Rev B 49:14251–14269
29. Kresse G, Furthmüller J (1996) Comput Mat Sci 6:15–50
30. Kresse G, Furthmüller J (1996) Phys Rev B 54:11169–11186
31. Perdew JP, Burke K, Ernzerhof M (1996) Phys Rev Lett 77:3865–3868
32. Perdew JP, Burke K, Ernzerhof M (1997) Phys Rev Lett 78:1396
33. Dudarev SL, Botton GA, Savrasov SY, Humphreys CJ, Sutton AP (1998) Phys Rev B 57:1505–1509
34. Grimme S (2006) J Comput Chem 27:1787–1799
35. Lutfalla S, Shapovalov V, Bell AT (2011) J Chem Theory Comput 7:2218–2223
36. Fu CL, Ho KM (1983) Phys Rev B 28:5480–5486
37. Blöchl PE (1994) Phys Rev B 50:17953
38. Kresse G, Joubert D (1999) Phys Rev B 59:1758–1775
39. Trifiro F, Grasselli RK (2014) Top Catal 57:1188–1195
40. McQuarrie DA, Simon JD (1999) Molecular thermodynamics. University Science Books, Sausalito, CA
41. Chang C-R, Zhao Z-J, Köhler K, Genest A, Li J, Rösch N (2012) Catal Sci Technol 2:2238–2248
42. Frisch MJ, Trucks GW, Schlegel HB, Scuseria GE, Robb MA, Cheeseman JR, Scalmani G, Barone V, Mennucci B, Petersson GA, Nakatsuji H, Caricato M, Li X, Hratchian HP, Izmaylov AF, Bloino J, Zheng G, Sonnenberg JL, Hada M, Ehara M, Toyota K, Fukuda R, Hasegawa J, Ishida M, Nakajima T, Honda Y, Kitao O, Nakai H, Vreven T, Montgomery JA Jr, Peralta JE, Ogliaro F, Bearpark MJ, Heyd J, Brothers EN, Kudin KN, Staroverov VN, Kobayashi R, Normand J, Raghavachari K, Rendell AP, Burant JC, Iyengar SS, Tomasi J, Cossi M, Rega N, Millam NJ, Klene M, Knox JE, Cross JB, Bakken V, Adamo C, Jaramillo J, Gomperts R, Stratmann RE, Yazyev O, Austin AJ, Cammi R, Pomelli C, Ochterski JW, Martin RL, Morokuma K, Zakrzewski VG, Voth GA, Salvador P, Dannenberg JJ, Dapprich S, Daniels AD, Farkas Ö, Foresman JB, Ortiz JV, Cioslowski J, Fox DJ (2009) Gaussian 09, Gaussian, Inc., Wallingford
43. Geupel S, Pilz K, Van Smaalen S, Bullesfeld F, Prokofiev A, Assmus W (2002) Acta Cryst C 58:i9–i13
44. Gautier R, Gautier R, Hernandez O, Audebrand N, Bataille T, Roiland C, Elkaïm E, Pollès L, Furet E, Fur E (2013) Dalton Trans 42:8124–8131
45. Girgsdies F, Schneider M, Brückner A, Ressler T, Schlögl R (2009) Solid State Sci 11:1258–1264
46. Chiu C, Genest A, Borgna A, Rösch N (2014) ACS Catal 4:4178–4188
47. Alexopoulos K, Reyniers M-F, Marin GB (2012) J Catal 289:127–139
48. Cheng M-J, Goddard WA (2013) J Am Chem Soc 135:4600–4603
49. Cheng M-J, Goddard WA, Fu R (2014) Top Catal 57:1171–1187
50. Miyamoto K, Nitadori T, Mizuno N, Okuhara T, Misono M (1988) Chem Lett 17:303–306
51. Centi G, Fornasari G, Trifiro F (1984) J Catal 89:44–51
52. Pepera MA, Callahan JL, Desmond MJ, Milberger EC, Blum PR, Bremer NJ (1985) J Am Chem Soc 107:4883–4892
53. Campbell CT, Sellers JRV (2012) J Am Chem Soc 134:18109–18115
54. Kozuch S, Shaik S (2008) J Phys Chem A 112:6032–6041
55. Kozuch S, Shaik S (2006) J Am Chem Soc 128:3355–3365
56. Rozanska X, Fortrie R, Sauer J (2014) J Am Chem Soc 136:7751–7761
57. Cheng M-J, Chenoweth K, Oxgaard J, van Duin A, Goddard WA (2007) J Phys Chem C 111:5115–5127
58. Rozanska X, Sauer J (2009) J Phys Chem A 113:11586–11594
59. Silversmit G, Depla D, Poelman H, Marin GB (2004) J Electron Spectrosc Relat Phenom 135:167–175
60. Coulston GW, Thompson EA, Herron N (1996) J Catal 163:122–129
61. Suchorski Y, Rihko-Struckmann L, Klose F, Ye Y, Alandjiyska M, Sundmacher K, Weiss H (2005) Appl Surf Sci 249:231–237
62. Kleimenov E, Bluhm H, Hävecker M, Knop-Gericke A, Pestryakov A, Teschner D, Lopez-Sanchez JA, Bartley JK, Hutchings GJ, Schlögl R (2005) Surf Sci 575:181–188
63. Dummer NF, Bartley JK, Hutchings GJ (2011) Adv Catal 54:189–247
64. Bartley JK, Dummer NF, Hutchings GJ (2009) In: Jackson SD, Hargreaves JSJ (eds) Metal oxide catalysis. Wiley, Hoboken, pp 499–537
65. Bordes-Richards E, Shekari A, Patience GS (2014) In: Duprez D, Cavani F (eds) Handbook of advanced methods and processes in oxidation catalysis, vol 1. Imperial College Press, London, pp 549–585
66. Carreon MA, Guliants VV (2011) In: Hess C, Schlögl R (eds) Nanostructured catalysts: selective oxidation. Royal Society of Chemistry, Cambridge, pp 141–168
67. Blanksby SJ, Ellison GB (2003) Acc Chem Res 36:255–263